Melting of two-dimensional tunable-diameter colloidal crystals

Y. Han,[*] N. Y. Ha,[†] A. M. Alsayed, and A. G. Yodh

Department of Physics and Astronomy, University of Pennsylvania, 209 South 33rd Street, Philadelphia, Pennsylvania 19104-6396, USA
(Received 12 February 2007; revised manuscript received 24 November 2007; published 18 April 2008)

Melting of two-dimensional colloidal crystals is studied by video microscopy. The samples were composed of microgel spheres whose diameters could be temperature tuned, and whose pair potentials were measured to be short ranged and repulsive. We observed two-step melting from the crystal to a hexatic phase and from the hexatic to the liquid phase as a function of the temperature-tunable volume fraction. The translational and orientational susceptibilities enabled us to definitively determine the phase transition points, avoiding ambiguities inherent in other analyses and resolving a "dislocation precursor stage" in the solid phase that some of the traditional analyses may incorrectly associate with the hexatic phase. A prefreezing stage of the liquid with ordered patches was also found.

I. INTRODUCTION

Two-dimensional (2D) melting is a classic problem in condensed matter physics [1], and, over the years, theories attempting to understand 2D melting have emphasized topological defects [2–5], geometrical defects [6], and grain boundaries [7]. The most popular model for understanding the transition is Kosterlitz-Thouless-Halperin-Nelson-Young (KTHNY) theory [2–5], which predicts two-step melting, from the crystal to a hexatic phase and then from the hexatic to a liquid phase. The intermediate hexatic phase has short-range translational and quasi-long-range orientational order, and the two transitions are beautifully characterized by the creation, binding, and unbinding of topological defects, i.e., dislocations and disclinations, respectively. Experimenters have sought out these features across a wide range of materials, including monolayers of molecules and electrons [1], liquid crystals [8], superconductors [9], diblock copolymers [10], and colloidal suspensions [11–16]. Some experiments and simulations have demonstrated substantial agreement with KTHNY theory, but others exhibit deviations and ambiguities possibly due to finite-size effects [1], the interaction range and form [16], and out-of-plane fluctuations [17,18]. In our view, the collection of evidence clearly points to the validity of the KTHNY scenario in 2D systems with long-range interaction potentials [13–15,19], but the evidence is less convincing in systems with short-range interactions [20–24]. Consequently it remains desirable to explore the phenomena in other model systems, especially those with short-ranged interactions.

In this paper we examine 2D melting in a colloidal system. The pair potential between particles in this colloidal suspension is *short ranged* and *repulsive*, and the sphere diameter is thermally sensitive, so that temperature tuning can be used to vary the sample volume fraction and drive the melting transition. Temperature-sensitive particles enable us

to follow the spatiotemporal evolution of the same sample area through the entire sequence of transitions. This feature is attractive and was not realized in previous colloidal melting experiments which employed samples composed of charged spheres in the wedge geometry with density gradients [11], nor in experiments that employed samples composed of hard spheres in many different concentration-dependent cells [12]. The temperature-sensitive samples employed herein start in the equilibrium crystal phase and reequilibrate rapidly after each tiny temperature jump. Therefore, they are unlikely to be trapped in metastable glassy states during melting. Beautiful recent experiments using magnetic spheres with tunable dipole-dipole interactions [13–15] share some of these advantages but also differ from the present experiments in a complementary way as a result of their long-range dipolar interactions.

We measured a variety of sample properties during melting, including radial distribution functions, structure factors, topological defect densities, dynamic Lindemann parameters [13], translational and orientational order parameters, and order parameter correlation functions in space and time. In this process we discovered that the order parameter susceptibility, i.e., the order parameter fluctuations, proved superior for finding phase transition points compared to other analyses which typically suffer finite-size and/or finite-time ambiguities. The susceptibility method has been applied in simulations [17,21], but to our knowledge has not been applied in imaging experiments. Using this method, we clearly resolved the intermediate hexatic phase, and we identified a "dislocation precursor stage" in the crystal phase that traditional analyses sometimes incorrectly assign to the hexatic phase. In addition, the functional form of the susceptibility near the phase transition points, e.g., divergences or discontinuities, can be used to determine the order of the phase transition.

II. EXPERIMENT

A. Sample preparation and characterization

The samples consisted of a monolayer of *N*-isopropyl acrylamide (NIPA) spheres confined between two glass coverslips. We synthesized NIPA microgel spheres by free-

---

[*]Present address: Department of Physics, Hong Kong University of Science and Technology, Clear Water Bay, Hong Kong.

[†]Present address: Department of Physics, Ajou University, Suwon 443-749, Korea.

radical polymerization [25] and suspended them in buffer solution (pH=4.0, 20 mM acetic acid). The NIPA polymer becomes less hydrophilic at high temperature [26], and therefore the sphere diameter decreases with increasing temperature as water moves out of the microgel particle. Dynamic light scattering measurements found the NIPA sphere hydrodynamic diameter to vary linearly from 950 nm at 20 °C to 740 nm at 30 °C and showed that sphere polydispersity was less than 3%. Such small polydispersity should not affect the nature of the melting process [27]. The cleaned glass surfaces were coated with a layer of 100-nm-diameter NIPA spheres to prevent particle sticking. A simple geometrical calculation showed that 100 nm close packed spheres on the surface give rise to ∼3 nm surface roughness for the 800-nm-diameter spheres. This surface roughness is negligible compared to sphere polydispersity and wall separation fluctuations. In addition, our observations of the large sphere motions at lower concentrations did not find evidence of preferential spatial locations, i.e., of significant surface potentials.

The dense monolayer of 800 nm spheres formed crystal domains within the sample cell of typical size ∼(40 μm)², corresponding to ∼3000 particles. Measurements were carried out on a ∼(20 μm)² central area away from the grain boundaries. In practice we found that grain boundaries affected only a few neighboring lines of particles, and that melting started from both inside crystal domains and at grain boundaries. This behavior differs qualitatively from grain-boundary melting in 3D [25] and edge melting in 2D [28], wherein melting starts from grain boundaries or edges and then propagates into the crystal. Our observations suggest that interfacial energies for liquid nucleation from anywhere within the crystal are similar to those near grain boundaries. It appears that melting starts nearly simultaneously throughout the crystal.

The sample was heated very slowly in 0.1 °C steps for a few minutes, and the measurements were taken after the temperature stabilized. We did not observe convection, even in samples with smaller particles at much lower volume fractions. The sample cell was approximately 1 μm thick, much smaller than the 1-mm-thick glass slide on which it was mounted. The temperature difference across the slide was about 5 °C, so the gradient across the sample was very small (<0.01 °C). Furthermore, the Reynolds number of water at this 1 μm scale is small, making convection unlikely. Before starting the measurements we cycled the samples once or twice above the melting point in order to relieve any possible shear stresses.

Particle motions were observed by microscope and recorded to videotape using a charge-coupled device camera operating at 30 frames/s. The particle positions in each frame were obtained from standard image analysis algorithms [29]. The temperature control (Bioptechs) on the microscope had slightly better than 0.1 °C resolution. We increased the temperature from 26.5 to 28.5 °C in 0.2 °C steps and recorded 5 min of video at each temperature after sample equilibration.

Particle interactions were directly quantified by measuring the particle radial distribution function $g(r)$ in a dilute (i.e., areal density $\rho \sim 10\%$) monolayer of spheres in the same sample cell. We corrected for image artifacts [30] at each
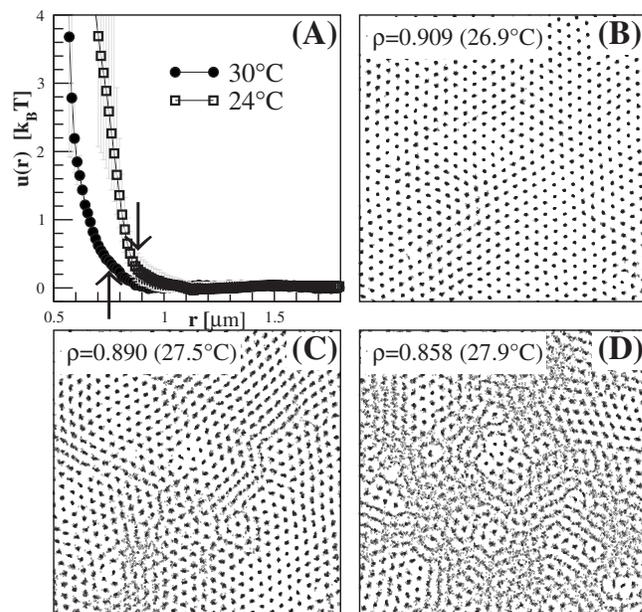

FIG. 1. (a) Pair potential $u(r)$ of NIPA spheres at 24 (squares) and 30 °C (circles). Arrows indicate corresponding hydrodynamic radius measured by dynamic light scattering. (b)–(d): Typical 10 s particle trajectories in the crystal, hexatic, and liquid phases, respectively.

temperature using the method described in Ref. [31]. From $g(r)$, we applied liquid structure theory to extract [32] the pair potentials $u(r)$ shown in Fig. 1. Note that the potentials are short ranged and repulsive. The effective particle diameter at $1k_BT$ is ∼10% smaller than the hydrodynamic diameter measured by dynamic light scattering. Herein we use the hydrodynamic diameter σ for defining the areal density $\rho = n\pi\sigma^2/4$, where n is the areal number density.

B. Order parameter correlations in space and time

Figures 1(b)–1(d) show typical particle trajectories in the three phases. In KTHNY theory, the traditional way to distinguish phases derives from the shapes of the order parameter correlation functions. For our analysis we first labeled each particle by $(x_j, y_j, t, \psi_{6j}, \psi_{Tj})$. Here t is time, $\psi_{6j} = (\sum_{k=1}^{nn} e^{6i\theta_{jk}})/\mathcal{N}$ is the orientational order parameter, and $\psi_{Tj} = e^{i\mathbf{G}\cdot\mathbf{r}_j}$ is the translational order parameter for particle j at position $\mathbf{r}_j = (x_j, y_j)$. θ_{jk} is the angle of the bond between particle j and its neighbor k. $\mathcal{N}$ is the number of nearest neighbors (NNs). $\mathbf{G}$ is a primary reciprocal lattice vector determined from the peak of the 2D structure factor $s(k)$ at each temperature. In the liquid phase $s(k)$ has no angular peak. Therefore we use $\mathbf{G}$ of the crystal phase to compute ψ_T in the liquid phase; this approach has been used previously [18,33]. The assignment of $\mathbf{G}$ is not always easy in the crystal or hexatic phase. To this end we maximized ψ_T at each temperature (including the liquid phase) by iteratively varying $\mathbf{G}$ around an initial estimate derived from $s(k)$; the resultant $\mathbf{G}$ was assumed to be optimal for that particular sample temperature and was used in subsequent calculations of order parameter correlation functions and the translational susceptibility.
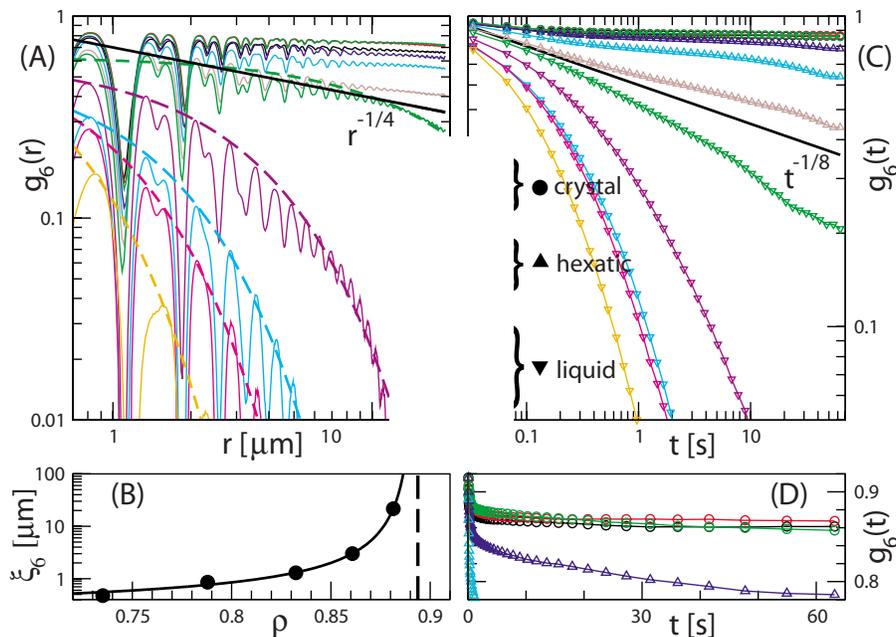
FIG. 2. (Color online) (a) Orientational correlation functions $g_6(r)$. Minima in the oscillations are associated with positions in the lattice that are not favored by particles. The five dashed curves are fits of $g_6(r)$ to e^{-r/ξ_6}. $r^{-1/4}$ is the KTHNY prediction at the hexatic-liquid transition point. (b) Circles are the orientational correlation lengths ξ_6 obtained from the fits in (a). The solid curve is a fit to the KTHNY prediction $\xi_6(\rho) \propto e^{-b/\sqrt{\rho_i-\rho}}$ with $b = 0.566$ and $\rho_i = 0.894$. These fit values, however, are prone to systematic error as a result of finite-size effects [34]. (c) Orientational correlation function $g_6(t)$ in time. $t^{-1/8}$ is the KTHNY prediction at hexatic-liquid transition point. (d) Expanded version of (c) that more clearly exhibits the transition from long-range to quasi-long-range order. The 11 temperatures correspond to the 11 densities in Fig. 7.

Correlations of ψ_6 and ψ_T in space and time are readily constructed, yielding four correlation functions

$$g_\Gamma(r = |\mathbf{r}_i - \mathbf{r}_j|) = \langle \psi_i^*(r_i)\psi_j(r_j) \rangle, \qquad (1a)$$

$$g_\Gamma(t) = \langle \psi_i^*(\tau)\psi_i(\tau + t) \rangle. \qquad (1b)$$

where $\Gamma = 6, T$. Note that $g_T(r)$ and $g_6(r)$ are two-body quantities, and $g_T(t)$ and $g_6(t)$ are one-body quantities.

From the $g_6(r)$ shown in Fig. 2(a), we can semiquantitatively distinguish three regimes corresponding to crystal, hexatic, and liquid phases as predicted by KTHNY theory: $g_6(r) \sim \text{const}$ (long-range orientational order) for 26.5–26.9 °C, $g_6(r) \sim r^{-\eta_{6r}}$ (quasi-long-range order) for 27.1–27.5 °C, and $g_6(r) \sim e^{-r/\xi_6}$ (short-range order) for 27.7–28.5 °C. These three regions are more clearly resolved over three decades of dynamic range in Figs. 2(c) and 2(d), which plot the dynamic quantity $g_6(t)$. Comparing Figs. 2(a) and 2(c), we confirm the KTHNY predictions [5] that the power law decay of $g_6(t)$ is two times slower than that of $g_6(r)$, and $2\eta_{6t} = \eta_{6r} = 1/4$ at the hexatic-liquid transition point. $g_T(t)$ and $g_T(r)$ yielded consistent results. For example, Fig. 3 shows that $g_T(t) \sim t^{-\eta_T}$ (crystal) for $T < 27$ °C and $g_T(t) \sim e^{-t/\tau}$ (hexatic and liquid) for $T \gtrsim 27$ °C. The KTHNY prediction that $\eta_{Tr} = 1/3$ [5] at the crystal-hexatic transition point was also confirmed. The oscillations in $g_6(r)$ and $g_T(r)$ correspond to the oscillations of the radial distribution function $g(r)$ in Fig. 4.

Despite substantial agreement with the KTHNY model, two major ambiguities arise in the traditional correlation function analyses: (1) The power law decay of g_6 can reflect crystal-liquid coexistence rather than the hexatic phase, and (2) finite-size and finite-time effects induce ambiguities in the correlation function curve shapes near transition points. For example, the $T = 27.7$ °C curve in Fig. 2(c) appears to decay algebraically over the finite measured time scale, but could decay exponentially at longer times. Since the curve appears below the theoretical $t^{-1/8}$ transition curve, we (perhaps reasonably) assigned the system to the liquid phase.
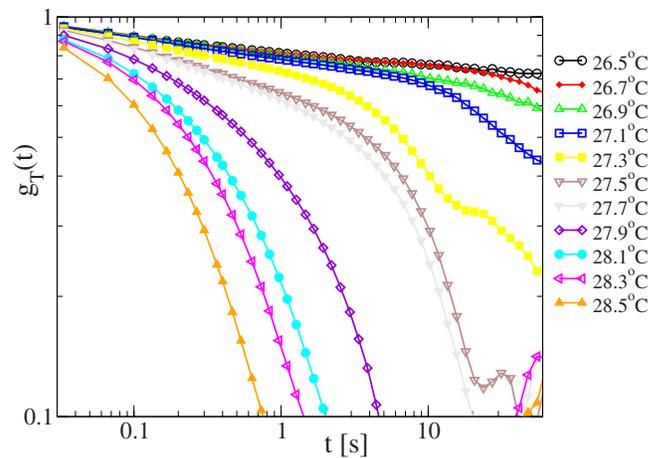

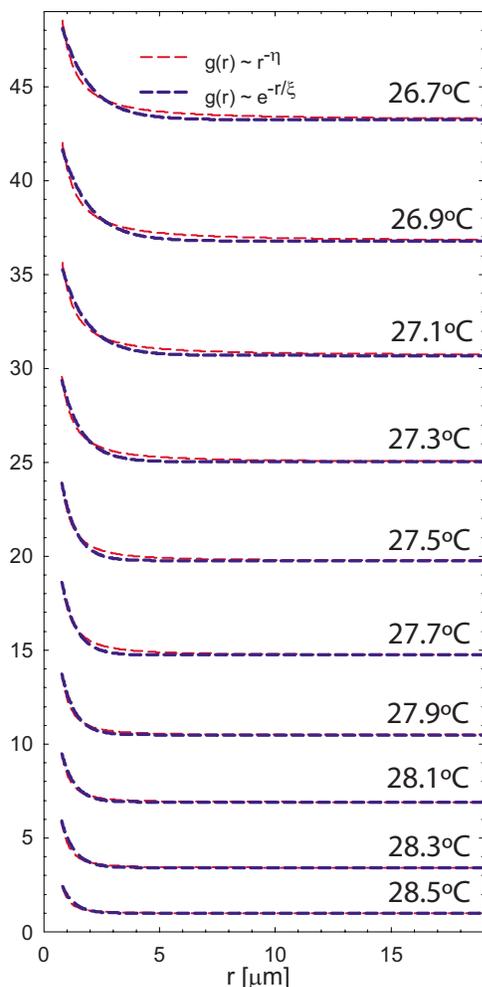FIG. 3. (Color online) Translational correlation functions $g_T(t)$ in time.

FIG. 4. (Color online) Radial distribution function $g(r)$ at different temperatures. Curves are shifted vertically for clarity. The thin red and thick blue dashed curves are the power law and the exponential fits, respectively.

C. Radial distribution functions and structure factors

Other correlation functions, such as the spatial density radial distribution function $g(r)$ in Fig. 4 and the 2D structure factor $s(k)$ in Fig. 5, also appeared to have ambiguities near phase transition points. The spatial density autocorrelation function, i.e., the radial distribution function, is defined as

$$g(r = |\mathbf{r}|) = \frac{1}{n^2}\langle \rho(\mathbf{r}' + \mathbf{r}, t)\rho(\mathbf{r}', t)\rangle, \qquad (2)$$

where $\rho = \Sigma_{j=1}^{N(t)} \delta(\mathbf{r} - \mathbf{r}_j(t))$ is the distribution of N particles in the field of view with area A, and $n = \langle \rho = \langle N / A$ is the areal density. The angular brackets denote an average over time and space. The power law fits the data better in the low-temperature crystal phase as shown in Fig. 4. However, both power law and exponential forms fit the data equally well at high temperatures. The 2D structure factors in Fig. 5 were obtained by Fourier transforming the 2D radial distribution functions before azimuthally averaging them to obtain $g(r)$. The expected functional forms of the angular intensity profile of $s(\mathbf{k})$ from theory are square-root Lorentzian for the
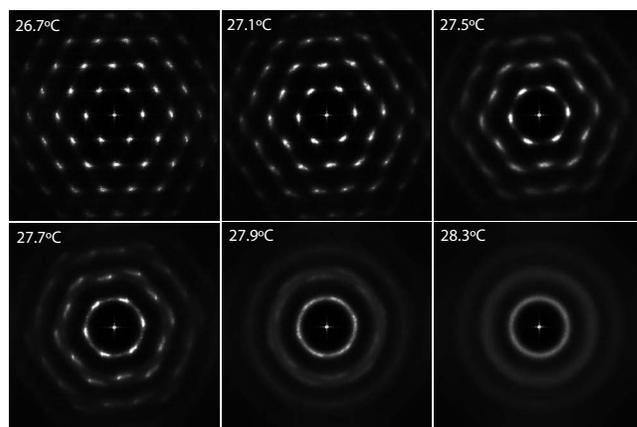

FIG. 5. 2D structure factors $s(\mathbf{k})$ at different temperatures.

hexatic phase and simple Lorentzian for the crystal phase [12,35]. However, the profiles become quite similar near the crystal-hexatic transition point, and we were unable to accurately determine the transition point from fits to $s(\mathbf{k})$.

D. Dynamic Lindemann parameter

Another function of interest is the Lindemann parameter, a traditional criterion of melting. For 2D melting, however, the Lindemann parameter diverges slowly even in the crystal phase due to strong long-wavelength fluctuations in 2D. We calculated the *dynamic* Lindemann parameter L [14], defined as

$$L^2 = \frac{\langle [\Delta \mathbf{r}_{\text{rel}}(t)]^2 \rangle}{2a^2} = \frac{\langle [\Delta \mathbf{u}_i(t) - \Delta \mathbf{u}_j(t)]^2 \rangle}{2a^2}, \qquad (3)$$

where $\Delta \mathbf{r}_{\text{rel}}$ is the relative neighbor-neighbor displacement, $\Delta \mathbf{u}_i$ is the displacement of particle i, and particles i and j are nearest neighbors. As shown in Fig. 6, L^2 converges below 27 °C; in this case particles remain near their lattice sites. Divergence of L^2 is found above 27 °C; in this case particles
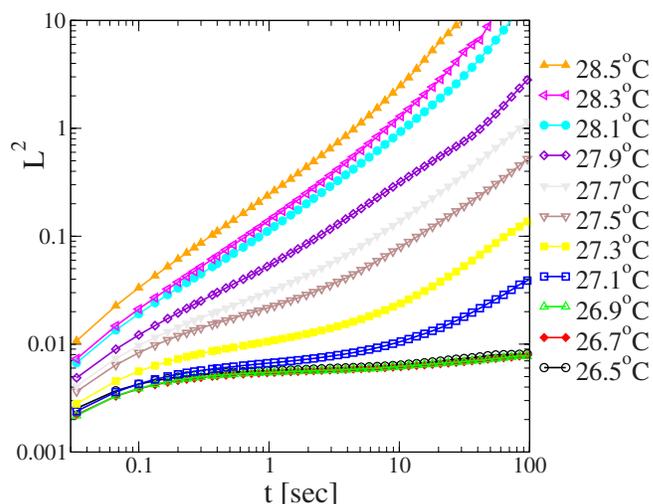

FIG. 6. (Color online) Square of the dynamic Lindemann parameters at 11 temperatures.
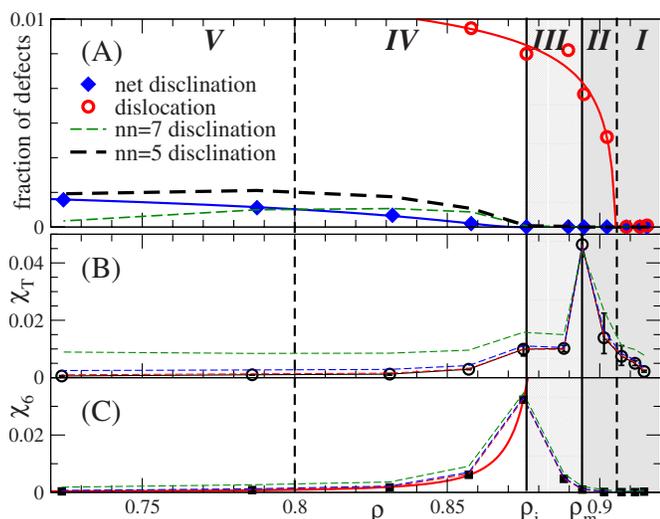
FIG. 7. (Color online) (a) Thick dashed curve: $\mathcal{N}=5$ disclination density. Thin dashed curve: $\mathcal{N}=7$ disclination density. Diamonds: net disclination density; Circles: dislocation density fitted by $e^{-2b_m/(\rho_m-\rho)^{0.36963}}$ [5]. (b) Translational and (c) orientational susceptibilities. Dashed curves: χ_L derived from subbox sizes L = 5, 10, 20 μm from top to bottom. Symbols: χ_∞ extrapolated from dashed curves. The solid curve in (c) is a fit to the KTHNY prediction [23] $\chi_6(\rho) \propto e^{-b_\chi/\sqrt{\rho_i-\rho}}$ with $\rho_i=0.901$, $b_\chi=1.14$. Vertical solid lines partition crystal (regions I and II), hexatic (region III), and liquid (regions IV and V) phases as determined from susceptibilities in (b) and (c). Region II is a dislocation precursor stage of the crystal with dislocations. Region IV is a prefreezing stage [36] of the liquid with ordered patches.

can more readily exchange positions with their neighbors via the gliding and climbing of dislocations [5]. This transition at 27 °C is consistent with our direct measurement of dislocation densities (see discussion below) in Fig. 7(a).

E. Defect densities and dynamics

Defect densities are helpful for distinguishing among different phases. Particles with $\mathcal{N}\neq6$ are considered to be defects. KTHNY theory suggests that the creation of *free* dislocations (isolated 5-7 pairs) drives the system from crystal to hexatic phase, and the creation of *free* disclinations (isolated $\mathcal{N}=5$ or 7 defects) drives the transition from the hexatic to the liquid phase. We measured defect concentrations as a function of temperature. Figure 7(a) shows that dislocations start to appear for T 27 °C (i.e., $\rho_m=0.905$), and disclinations start to appear for T 27.7 °C (i.e., $\rho_i=0.875$). Although defect density measurements are less sensitive to finite-size effects than the correlation functions [34], the assignment of a melting volume fraction ρ_m based on defect density [Fig. 7(a)] is somewhat problematic. Problems can arise because (1) the data [Fig. 7(a)] inevitably include dislocations that are not completely "free," e.g., the dislocation pairs in Fig. 8(a), that are nearly adjacent to one another, point in opposite directions, and thus give zero Burgers vector for a large Burgers circuit, and (2) the data [Fig. 7(a)] are susceptible to other systematic errors, e.g., miscounting large defect clusters as equivalent to a free dislocation (e.g., a
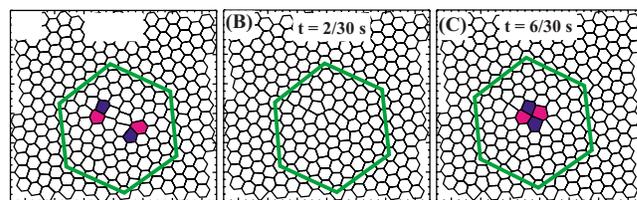

FIG. 8. (Color online) Voronoi diagram of the time evolution of a nonfree dislocation pair at 27.1 °C. Dark blue and light red represent particles with five and seven nearest neighbors, respectively. (a), (b), and (c) all yield zero Burgers vector as shown by the closed hexagonal loop. Dislocations can rapidly form and annihilate in pairs, if they are in the same lattice line.

"free" 6-mer 5–7-5–7-5–7). In fact, Fig. 7(a) very likely overestimates ρ_m because sufficient numbers of nonfree dislocations are needed before the dislocation chemical potential reaches zero and free dislocations are produced. Consequently, a dislocation precursor stage in the crystal phase might be expected.

We also observed more $\mathcal{N}=8,9$ than $\mathcal{N}=3,4$ defects. This imbalance compensated for some of the density difference between five and seven NNs. In fact, a small imbalance in five and seven NN disclinations might be expected. The concentration equality holds only in perfect crystals with *periodic* boundary conditions and neglecting $\mathcal{N}=3,4,8,\ldots$ defects [5]. Our samples have free boundary conditions. Periodic boundary conditions create an artificial constraint that forces vacancies and interstitials to be created in pairs rather than diffusing in from the surface [5]. For similar reasons, the densities for five and seven NNs are different in our experiment, but are usually observed to be the same in simulations (e.g., [18]). Furthermore, any deviation from the strict monolayer limit can produce a concentration asymmetry [5].

Besides the static properties noted above, we observed some interesting defect dynamics. For example, dislocations often dissociated from larger defect clusters (e.g., 6-mer 5–7-5–7-5–7) rather than from isolated pairs of dislocations (the 5–7-5–7 quartet), perhaps because the energy change for such disassociation is small.

F. Susceptibilities

In order to avoid the ambiguities outlined above and determine the true ρ_m, we explored the utility of another method for finding phase transition points. This method is based on the order parameter fluctuations and is characterized by the order parameter susceptibility

$$\chi_L = L^2(\langle|\psi^2|\rangle - \langle|\psi|\rangle^2). \tag{4}$$

Here L is the system size, $=6,T$, and $\psi = (\Sigma_{i=1}^N \psi_i)/N$ is the *total* order parameter averaged over all N particles in the $L\times L$ box. For example, χ_T measures the response of the translational order parameter to sinusoidal density fluctuations with periodicity characterized by **G**. χ is a measure of the fluctuations of the order parameter in 9000 frames. To ameliorate finite-size effects, we calculated χ_L in different size subboxes within the sample [dashed curves in Figs. 7(b) and 7(c)] and then extrapolated to χ_∞, thus attaining the ther-

modynamic limit. The χ_L of small subboxes were noisy due to statistics; thus before calculating χ_L, we randomized each particle's (x_j, y_j) position within the $(20 \ \mu\text{m})^2$ box while leaving its $(t, \psi_{j6}, \psi_{jT})$ untouched. Such position randomization did not affect χ_L in the largest box, but smoothed χ_L in subboxes, averaging over spatial fluctuations while preserving time fluctuations. Without such a spatial average, the dashed curves in Figs. 7(b) and 7(c) became noisier, but the same transition points (diverging points) were resolved. The experimental noise is estimated as the standard deviation of ψ_T in different time frames with respect to the mean $\langle \psi_T \rangle$. The error bars in Fig. 7(b) are estimated from deviations of **G** that gave the same noise as found for ψ_T.

The sharp divergence or discontinuity of $\chi_{T\infty}$ and $\chi_{6\infty}$ in Figs. 7(b) and 7(c) clearly indicate the two transitions of the melting process. Although the magnitude of χ suffered from size effects, the divergence point of χ was robust to box size. Thus the susceptibility method avoided finite-size ambiguities. The divergence of χ also avoids ambiguities arising from the similar functional forms of other measures (e.g., correlation functions) near transition points. Theoretically we expect the divergence of χ to have better statistics than the correlation function shape, because χ is essentially an integral of the correlation function. We also observed that the divergence points of the susceptibilities were robust to small uncertainties in **G**, although the exact magnitude of χ_T was somewhat sensitive to **G**.

G. Five regimes

Five regimes are marked off in Fig. 7 based on the various analyses we have carried out. Region I is crystal with few dislocations [Fig. 7(a)], convergent dynamic Lindemann parameters over the measured time scales (Fig. 6), constant $g_6(r)$ and $g_6(t)$ (Fig. 2), and algebraic decay of $g_T(t)$ (Fig. 3). We take region II to be a dislocation precursor stage in the crystal because dislocations have started to appear, but their density is not high enough for the system to reach the hexatic phase, wherein the chemical potential of dislocation reaches zero. In other words, the observed dislocations in region II are not free. This gas of nonfree dislocations causes a softening of the crystal, an effect which has been observed in the crystal phase [37]. The dynamic Lindemann parameter is divergent in region II, a direct consequence of the nonzero dislocation density, which permits particles near dislocations to diffuse out of their cages via the gliding and climbing [5] of dislocations. The correlation function $g_6(t)$ has finite-size ambiguity in region II. For example, the $T = 27.1$ °C curve in Fig. 2(d) appears to have lost orientational order over the measured time scale, but could become constant at longer times. If correlation measurements are accurate, then part or all of the precursor stage II can be correctly assigned to be in the crystal phase; see Ref. [37]. Interestingly, Li has reanalyzed the simulation data in Ref. [18] with susceptibilities and has also observed the dislocation precursor stage [38].

Region III is the hexatic phase as determined from the χ measurements and other analyses. In region IV, disclinations start to appear [Fig. 7(a)], and $g_6(r)$ and $g_6(t)$ decay exponentially (Fig. 2). We take region IV to be a prefreezing stage (Fig. 2). We take region IV to be a prefreezing

liquid [36] because it has visible ordered patches. The nonzero ψ_6, the splitting of the second peak in $g(r)$, and the hexagonal shape of $s(k)$ in region IV also are indicative of the presence of ordered patches. Such ordered patches have been observed in simulations [38], but we are not aware of reports of a prefreezing stage in 2D melting experiments, perhaps because it is well known that ordered clusters often exist in dense fluids. Region V is the liquid phase.

H. Phase transition order

The order of the phase transition can, in principle, be deduced from the shape of the susceptibility curves. If the curve on the left of the diverging point and the curve on the right of the diverging point have the same asymptotic ρ, then the transition is second order; otherwise, it is first order [39]. The curve shape in Figs. 7(b) and 7(c) are consistent with second-order transitions. However, the χ_T curve shape is sensitive to the choice of **G** even though the divergence point is quite robust. For example, using **G** of the crystal for all temperatures yielded a curve shape that appeared more like a first-order transition.

For the liquid-hexatic transition in Fig. 7(c), when we fitted the left part (liquid regime) of the curve with the KTHNY prediction, we obtained an unreasonably high asymptotic transition density $\rho_i = 0.901$ [21]. This discrepancy suggests that the hexatic-liquid transition may be more first-order-like. In addition, the continuous phase transitions must satisfy universality relations, while first-order transitions need not. Our $b_6 = 0.566$, from Fig. 2(b) and $b_{6\chi} = 1.14$, from Fig. 7(c) do not completely satisfy the universality [23] $b_{6\chi} = (2 - \eta_6)b_6$ where $\eta_6 = 1/4$. This failure could be viewed as further evidence of a first-order transition; however, when we forced $b_{6\chi}$ and b_6 to satisfy the universality relation, they still gave somewhat reasonable (albeit worse) fitting curves because other fitting parameters were adjustable too. For example, the five data points in Fig. 2(b) can be fitted well by the other two free parameters when b_6 is fixed. In total, the evidence leans slightly to favoring a first-order liquid-hexatic transition, but is not sufficient to unambiguously exclude a second-order transition. Future work with finer control of the approach to the phase transition should enable us to pin down the order of the two transitions more precisely.

III. CONCLUSIONS

In summary, we used the divergence of susceptibilities to determine the phase transition points of a 2D colloidal suspension during the melting process. This approach avoided ambiguities from finite-size effects and the divergence points were robust. We clearly observed the hexatic phase in a system of particles interacting via short-range soft-repulsion potentials. Five regimes were assigned to the phase diagram in Fig. 7. A number of KTHNY predictions were quantitatively confirmed, especially near the hexatic-liquid transition, but the order of the two phase transitions was not unambiguously resolved due to our limited temperature resolution.

ACKNOWLEDGMENTS

[1] K. J. Strandburg, Rev. Mod. Phys. **60**, 161 (1988).

[2] J. M. Kosterlitz and D. J. Thouless, J. Phys. C **6**, 1181 (1973).

[3] D. R. Nelson and B. I. Halperin, Phys. Rev. B **19**, 2457 (1979).

[4] A. P. Young, Phys. Rev. B **19**, 1855 (1979).

[5] D. R. Nelson, *Defects and Geometery in Condensed Matter Physics* (Cambridge University Press, Cambridge, U.K., 2002).

[6] M. A. Glaser and N. A. Clark, Adv. Chem. Phys. **83**, 543 (1992) ; Y. Lansac, M. A. Glaser, and N. A. Clark, Phys. Rev. E **73**, 041501 (2006).

[7] S. T. Chui, Phys. Rev. Lett. **48**, 933 (1982); Phys. Rev. B **28**, 178 (1983).

[8] C. F. Chou, A. J. Jin, S. W. Hui, C. C. Huang, and J. T. Ho, Science **280**, 1424 (1998).

[9] D. G. Grier, C. A. Murray, C. A. Bolle, P. L. Gammel, D. J. Bishop, D. B. Mitzi, and A. Kapitulnik, Phys. Rev. Lett. **66**, 2270 (1991).

[10] D. E. Angelescu, C. K. Harrison, M. L. Trawick, R. A. Register, and P. M. Chaikin, Phys. Rev. Lett. **95**, 025702 (2005).

[11] C. A. Murray and D. H. Van Winkle, Phys. Rev. Lett. **58**, 1200 (1987).

[12] A. H. Marcus and S. A. Rice, Phys. Rev. Lett. **77**, 2577 (1996).

[13] K. Zahn, R. Lenke, and G. Maret, Phys. Rev. Lett. **82**, 2721 (1999).

[14] K. Zahn and G. Maret, Phys. Rev. Lett. **85**, 3656 (2000).

[15] H. H. von Grünberg, P. Keim, K. Zahn, and G. Maret, Phys. Rev. Lett. **93**, 255703 (2004); H. H. von Grünberg, P. Keim, and G. Maret, Soft Matter **3**, 41 (2007).

[16] P. Karnchanaphanurach, B. H. Lin, and S. A. Rice, Phys. Rev. E **61**, 4036 (2000).

[17] R. Zangi and S. A. Rice, Phys. Rev. E **58**, 7529 (1998).

[18] D. Li and S. A. Rice, Phys. Rev. E **72**, 041506 (2005).

[19] S. Z. Lin, B. Zheng, and S. Trimper, Phys. Rev. E **73**, 066106 (2006).

[20] J. A. Zollweg and G. V. Chester, Phys. Rev. B **46**, 11186 (1992).

[21] H. Weber, D. Marx, and K. Binder, Phys. Rev. B **51**, 14636 (1995).

[22] J. F. Fernandez, J. J. Alonso, and J. Stankiewicz, Phys. Rev. Lett. **75**, 3477 (1995).

[23] A. Jaster, Europhys. Lett. **42**, 277 (1998).

[24] A. Jaster, Phys. Lett. A **330**, 120 (2004).

[25] A. M. Alsayed, M. F. Islam, J. Zhang, P. J. Collings, and A. G. Yodh, Science **309**, 1207 (2005).

[26] R. Pelton, Adv. Colloid Interface Sci. **85**, 1 (2000).

[27] S. Pronk and D. Frenkel, Phys. Rev. E **69**, 066123 (2004).

[28] J. G. Dash, Rev. Mod. Phys. **71**, 1737 (1999); Contemp. Phys. **43**, 427 (2002).

[29] J. C. Crocker and D. G. Grier, J. Colloid Interface Sci. **179**, 298 (1996).

[30] J. Baumgartl and C. Bechinger, Europhys. Lett. **71**, 487 (2005).

[31] M. Polin, D. G. Grier, and Y. Han, Phys. Rev. E **76**, 041406 (2007).

[32] S. H. Behrens and D. G. Grier, Phys. Rev. E **64**, 050401(R) (2001); Y. Han and D. G. Grier, Phys. Rev. Lett. **91**, 038302 (2003).

[33] H. Pang, Q. Pan, and P. H. Song, Phys. Rev. B **76**, 064109 (2007); D. S. Chekmarev, D. W. Oxtoby, and S. A. Rice, Phys. Rev. E **63**, 051502 (2001); C. Udink and J. van der Elsken, Phys. Rev. B **35**, 279 (1987).

[34] F. Celestini, F. Ercolessi, and E. Tosatti, Phys. Rev. Lett. **78**, 3153 (1997).

[35] S. C. Davey, J. Budai, J. W. Goodby, R. Pindak, and D. E. Moncton, Phys. Rev. Lett. **53**, 2129 (1984); G. Aeppli and R. Bruinsma, *ibid.* **53**, 2133 (1984).

[36] A. R. Ubbelohde, *Melting and Crystal Structure* (Clarendon, Oxford, 1965).

[37] H. H. von Grünberg, P. Keim, K. Zahn, and G. Maret, Phys. Rev. Lett. **93**, 255703 (2004); P. Keim, G. Maret, and H. H. von Grünberg, Phys. Rev. E **75**, 031402 (2007).

[38] D. Li (private communication).

[39] K. Binder, Rep. Prog. Phys. **50**, 783 (1987).